Research Article | Vol. 28, No. 16 / 3 August 2020 / Optics Express 23374
Optics EXPRESS

Laser-induced ultrasonics for detection of low-amplitude grating through metal layers with finite roughness

STEPHEN EDWARD,[1,2,4] HAO ZHANG,[1] STEFAN WITTE,[1,3] AND PAUL C. M. PLANKEN[1,2,5]

[1]Advanced Research Center for Nanolithography (ARCNL), Science Park 106, 1098 XG Amsterdam, The Netherlands
[2]Van der Waals-Zeeman Institute, University of Amsterdam, Science Park 904, 1098 XH Amsterdam, The Netherlands
[3]Department of Physics and Astronomy, Vrije Universiteit, De Boelelaan 1081, 1081 HV Amsterdam, The Netherlands
[4]sedward@arcnl.nl
[5]planken@arcnl.nl

Abstract: We report on the use of laser-induced ultrasonics for the detection of gratings with amplitudes as small as 0.5 nm, buried underneath an optically opaque nickel layer. In our experiments, we use gratings fabricated on top of a nickel layer on glass, and we optically pump and probe the sample from the glass side. The diffraction of the probe pulse from the acoustic echo from the buried grating is measured as a function of time. We use a numerical model to show how the various physical phenomena such as interface displacement, strain-optic effects, thermo-optic effects, and surface roughness influence the shape and strength of the time-dependent diffraction signal. More importantly, we use a Rayleigh-Rice scattering theory to quantify the amount of light scattering, which is then used as in input parameter in our numerical model to predict the time-dependent diffracted signal.

1. Introduction

Laser-induced ultrasound is ideal for sub-surface imaging and metrology as it can propagate through optically opaque materials and have extremely high frequencies, enabling the inspection of micro/nano-meter size features with high resolution [1–23]. The ability of acoustic waves to propagate through layers that are not transparent to light has led to applications in many fields, such as biomedical imaging [23–27], material characterisation [28–30], defect inspection in the manufacturing industry [31] and non-destructive testing [32]. For instance, in the semiconductor device manufacturing industry, a silicon wafer is aligned inside a nanolithography machine with an optical sensor that emits light and records optical diffraction from gratings etched in the silicon wafer. By knowing the phase and intensity of the +1 and -1 order diffracted light, the wafers can be aligned with sub-nanometer accuracy [33]. The need for high-density memory chips has pushed the industry to make new 3D NAND memory chips where memory cells are stacked on top of each other [34–37]. Very often opaque layers are deposited on top of these diffraction gratings during the fabrication of a 3D NAND memory chip and the current optical sensors inside nanolithography machines have difficulty detecting the gratings etched in the Si wafer.

Recently, we demonstrated it is possible to detect gratings buried underneath optically opaque metal and 20 dielectric layers using laser-induced, extremely-high frequency acoustic waves. In those experiments, the presence of a buried grating is detected by optical diffraction from an acoustic copy of the buried grating [38]. However, the buried gratings had a fixed, relatively large peak-to-valley amplitude of 10 nm and little is known about the limitations of this technique, in

#398134 https://doi.org/10.1364/OE.398134
Journal © 2020 Received 22 May 2020; revised 9 Jul 2020; accepted 15 Jul 2020; published 22 Jul 2020

Optics EXPRESS

particular, the sensitivity of the technique to detect very small amplitude buried gratings. Since the acoustic wave generated in metals contains ultra-high frequencies, it has the potential to detect shallow buried gratings with amplitude smaller than 10 nm.

Here,we show that laser-induced ultrasonics in an ultrafast pump-probe scheme can be used to detect the presence of very shallow gratings, down to 0.5 nm in amplitude, buried under optically opaque nickel (Ni) layers (Fig. 1). In our experiments, a single femtosecond pump-pulse from a low repetition rate laser launches an acoustic wave in a 130 nm thick Ni layer. The acoustic wave propagates through the Ni layer and reflects off a low-amplitude buried Ni grating. The acoustic wave propagates through the Ni layer and reflects off a low-amplitude buried Ni grating. Upon reflection, the wavefront of the acoustic wave acquires a spatially periodic phase, which can be viewed as an acoustic copy of the buried grating. The grating-shaped acoustic wave returns to the glass-metal interface, deforming the interface in a spatially periodic manner. A time-delayed femtosecond laser pulse illuminates this grating and the first-order diffracted signal is recorded as a function of pump-probe delay. The fact that we observe a time-dependent diffraction signal in itself is proof that the shape of the buried grating is encoded as a spatially periodic time delay on the acoustic wavefront. We use a complex 2D numerical model that includes the acoustic wave generation, propagation, and detection to predict the signal shapes in our measurements [39]. The numerically calculated diffraction signals are in excellent agreement with our measurements on all of the samples. We show that the strength and shape of the time-dependent diffraction signals are dependent on the amplitude of the buried grating. We also describe and quantify the different physical effects including interface displacement, strain-optic effects, thermo-optic effects, and interface scattering that cause the time-dependent diffraction signals and explain how each one influences the shape of the diffracted signal. From the measurements on the sample with smaller-amplitude buried gratings, we find that interface roughness plays a very significant role. Light scattered due to the interface roughness interferes with the light diffracted from the acoustic wave-induced gratings and leads to constructive/destructive interference which changes the shape and amplitude of the measured diffracted signal.

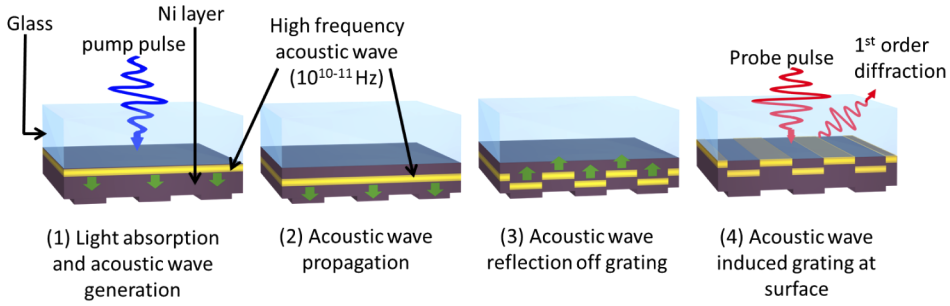

Fig. 1. Schematic explaining the detection of buried gratings using laser-induced ultrasonics. The femtosecond laser pulse is absorbed by the material at the substrate-material interface (1), which launches an acoustic wave that propagates through different layers (2). The acoustic wave reflects of the buried grating and returns to the substrate-material interface as a grating-shaped acoustic wave (3). The time-delayed femtosecond probe pulse diffracts of this interface grating, and the first-order diffraction signal is recorded (4).

2. Experimental Setup

A schematic of the pump-probe setup used for the experiments is shown in Fig. 2. A Ti:Sapphire multi-pass amplifier generates 30 fs pulses with a low repetition rate of 1 kHz and with a wavelength centered at 800 nm. A 95/5 beam splitter splits the output in two. The stronger beam is frequency-doubled to generate 400 nm pump pulses, and the weaker 800 nm beam is used as a

Optics EXPRESS

probe pulse. The pump pulse passes through a 500 Hz chopper, which blocks every alternate pump pulse. Both pump and probe are weakly focused onto the sample. The pump beam has a spot size of 500 μm, while the probe beam has a spot size of 250 μm on the sample.

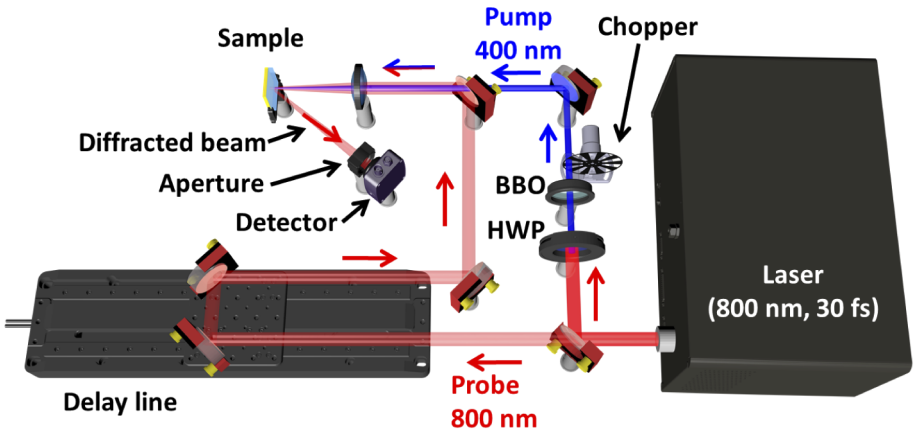

Fig. 2. Schematic of the experimental setup. The frequency-doubled 400 nm pump pulse is focused onto the sample and the 800 nm probe pulse that diffracts off the "copy" of the buried grating is recorded by the detectors while the delay line is used to change the pump-probe delay

Our samples consist of Ni gratings fabricated on top of a 130 nm thick flat Ni layer on a glass substrate. The samples are illuminated from the substrate side. This means that the pump and the probe illuminate the flat side of the Ni layer and thus, cannot "see" the grating as the penetration depth of both pump and probe are much smaller than the thickness of the metal layer. A delayed probe pulse diffracts from the acoustic wave-induced grating and is recorded by a Si-photodiode placed at an angle where the first-order diffracted pulse is expected. The delay between the pump and the probe is varied using a mechanical delay line. The measured signal is the diffracted probe signal recorded by the detector when the chopper blocks the pump beam subtracted from the diffracted probe signal when the pump beam is transmitted by the chopper. This is done to select only the pump-induced changes to the diffracted signal. Every single optical pump-pulse launches an acoustic wave and, combined with the low repetition rate of the laser, this means that the sound wave generated by a pulse has no interaction with the next one. Thus the system does not act like a forced oscillator.

All of the samples were fabricated with a pitch of 6 μm on a 130 nm thick flat Ni layer. The Ni layer was deposited on a glass substrate using electron beam evaporation, and the thickness was monitored using a calibrated quartz crystal monitor. On top of the flat Ni layer, Ni gratings were fabricated by UV lithography.

3. Results and discussion

3.1. Pump-probe experiments and simulation

We performed pump-probe experiments on four different samples with different Ni grating amplitudes of 12, 6, 2, and 0.5 nm. In Fig. 3 (bottom four panels), we plot the measured diffracted signal of these samples as a function of pump-probe delay (red curves). In the top panel, we show the measurement on a 130 nm thick layer of Ni without buried grating. All of the curves are vertically displaced for clarity. Except for the top panel, all the measured curves (red) are vertically scaled to match the calculated curves (blue). For the bottom four plots, we observe that the measured diffracted signal remains zero for approximately 35-40 ps, rising to a maximum at

Optics EXPRESS

46±1 ps. This peak is also the maximum of the time-dependent diffraction signal. After 65 ps, we observe a diffraction signal that is quasi-periodic and persists for more than 700 ps, where the shape and strength vary depending on the amplitude of the buried grating. In the measurements on the 2 and 0.5 nm amplitude buried grating samples, we observe a signal that periodically goes below the value observed at negative time delays. The signals from the measurements on 12 and 6 nm amplitude buried grating samples show a quasi-periodic oscillation that is superimposed on a gradually increasing signal.

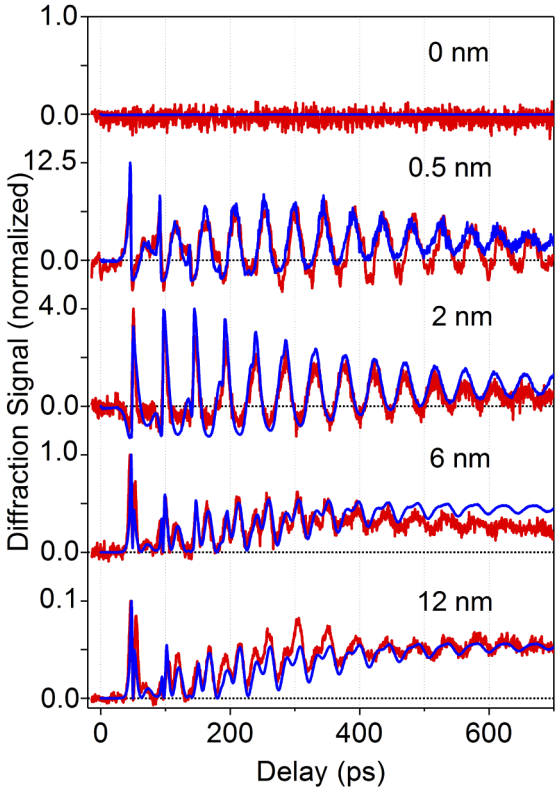

Fig. 3. The red curves are the experimentally measured diffracted probe signals plotted as a function of pump-probe delay for five gratings fabricated on 130 nm thick Ni layer. Different panels show the measured signal from gratings with an amplitude of 12 nm, 6 nm, 2 nm, 0.5 nm, and 0 nm. The pitch of all gratings is 6 µm. The blue curves are the numerically calculated diffraction signals as a function of pump-probe delay for each sample.

The fact that we observe a diffracted signal implies that we are able to detect the presence of buried gratings by diffracting the probe pulse from an acoustic "copy" of the buried grating at the glass-Ni interface. Our measurements show that we can detect extremely shallow buried gratings with an amplitude as low as 0.5 nm underneath an optically opaque Ni layer using laser-induced ultrasonics. In all of the measurements on buried gratings, we would expect the first reflection from the buried grating to arrive at the glass-Ni interface at 46±1 ps. For a 130 nm thick Ni layer, the round trip time of the acoustic wave can be calculated as $T = 2l/v$, where l is the layer thickness and v is the speed of sound in the metal. Assuming a longitudinal velocity of 5.8 km/s [4], the round trip time is expected to be 45 ps, which is close to the position of the first diffracted signal peak we observe in our measurements.

To better understand the measured time-dependent diffracted signals, we performed numerical simulations using an advanced 2D model developed in our group [39]. The model consists of a set

Optics EXPRESS

of equations that describes the generation, propagation, and optical detection of high-frequency acoustic waves. The numerically calculated diffraction signal is shown by the blue curves in the same graph (Fig. 3) for all five samples. Material parameters of the glass substrate and nickel were mostly taken from literature (Table 1). Unknown parameters such as the strain-optic coefficient and the thermo-optic coefficient, are manually adjusted until the best fit between the measurements and the calculations was obtained. Once the optical and material parameters were fixed, calculations were performed for the samples with different buried grating amplitude. We find that our simulations are in excellent agreement with the measurements.

Table 1. Material properties of the glass substrate and Ni, used in our calculations [4,21,40,41].

	Glass substrate	Ni
Optical penetration depth at 400 nm (nm)	N/A	12
Optical penetration depth at 800 nm (nm)	N/A	13
Electron-phonon coupling constant (10^{16}Wm^{-3}K^{-1})	3.2	36
Acoustic velocity (m/s)	5700	5800
Acoustic Impedance (10^{6}Ns/m^{3})	14.3	51.5

To identify the various physical mechanisms contributing to the measured diffracted signals, we show in Fig. 4 the various factors contributing to the calculated diffraction signal for (i) the 2 nm amplitude buried grating on 130 nm thick Ni (Fig. 4(a)) and, (ii) the 12 nm amplitude buried grating on 130 nm thick Ni (Fig. 4(b)). Although we can show the contributing factors for all of the buried grating samples, we have selected the 2, and 12 nm amplitude buried grating samples to highlight the difference in the relative contribution of different factors for these two samples. In Figs. 4(a) and 4(b), we plot the calculated diffraction signal from this sample from *only* the (i) displacement of the glass-Ni interface by the "grating-shaped" acoustic echo in Ni (green panels), (ii) changes in the optical constants of the glass due to the strain-optic effect (blue panels), (iii) changes in the optical constants of Ni due to the strain-optic effect (magenta panels), (iv) changes in the optical constants of the Ni due to the thermo-optic effect (yellow panels), (v) scattering from random surface roughness at the Ni-glass interface (orange panels). All of these plots are divided by the maximum value calculated for the black curve in the green panel of Fig. 4(a). For the ease of comparison, in the top panel, we show the measured diffracted signals (red curves) and the calculated diffracted signal, including all contributions (blue curves) for the same sample. The top panel in Figs. 4(a) and 4(b) are same as the 3rd and 1st panel from the bottom in Fig. 3, respectively. We now discuss the different factors that influence the strength and shape of the time dependent diffraction signal.

In our experiments, the length of the acoustic wave is expected to be a few tens of nanometers. Since we use 30 fs pump pulses, the length of the acoustic wave is determined by the combined effects of the optical penetration depth and the diffusion depth of the electron energy. Due to the high electron-phonon coupling strength in Ni, the hot electron gas formed by the pump pulse quasi-instantaneously heats up the lattice before it can diffuse much deeper into the material. However, if the optical pulse duration were larger than the time scale of electron gas cooling by electron-phonon coupling (which is about 1 ps in Ni), we expect the length of the acoustic wave to be determined by the optical pulse duration.

Optics EXPRESS

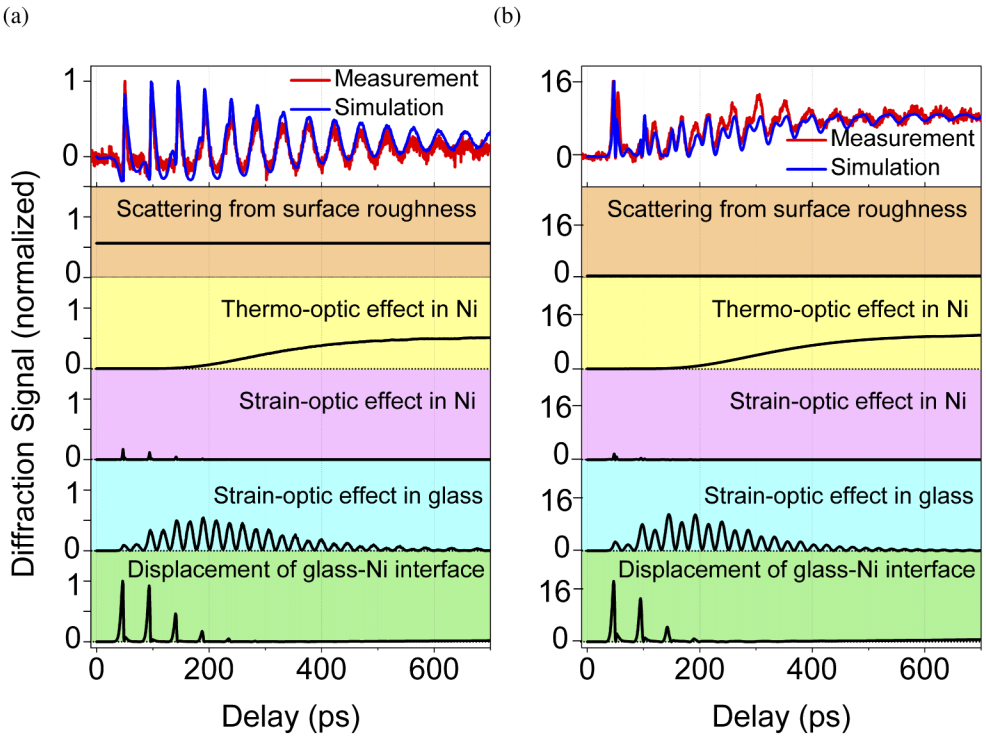

Fig. 4. (a) The top panel shows the measured and numerical calculated diffraction signal for the same sample when all factors are taken into account. The bottom 5 panels show the numerically calculated diffraction signal if only one factor contributing to the diffraction signal is taken into account for the sample with a 2 nm amplitude grating fabricated on 130 nm Ni. (b) Same as (a) but for the sample with a 12 nm amplitude grating fabricated on 130 nm Ni.

3.2. Displacement of glass-Ni interface

The acoustic wave generated in Ni at the glass-Ni interface propagates through the thick Ni layer, reflects off the buried grating, and returns to the glass-Ni interface as a grating-shaped echo. The acoustic echo displaces the atoms at the glass-Ni interface leading to an extremely shallow physical grating with an amplitude of few picometers only, having the same pitch as the buried grating. The peak-to-valley amplitudes of the displacement grating at the time delay where we observe the maximum diffraction efficiency, are 8 and 34 pm for the sample with 2 and 12 nm buried grating amplitudes, respectively. The acoustic wave undergoes multiple round trips inside the Ni layer, and a grating is formed each time the acoustic wave reaches the glass-Ni interface. The probe pulse diffracts from this grating and results in peaks in the diffraction signal that are separated by 46 ps, which is the acoustic round trip time inside the 130 nm Ni layer using the sound velocity in Ni of 5.8 km/s. This can be seen in the bottom panel of Figs. 4(a) and 4(b), where we observe peaks in the diffracted signal from multiple acoustic echoes, all separated by about 46 ps. Upon every reflection at the glass-Ni interface, 68% of the acoustic wave energy reflects back into the Ni layer. The partial transmission of acoustic energy into the glass is responsible for the decay of the sound wave inside the Ni.

Note that it is possible to generate surface plasmon polaritons at the interface of glass and some metals when such an interface is excited with a femtosecond laser pulse at the so-called plasmon resonance angle. However, in our experiments, we pump and probe the sample at normal

Optics EXPRESS

incidence and, therefore, no plasmonic effects are expected. The optical field incident on the metal does have a finite penetration depth of about 13 nm, and this is fully taken into account in the numerical model that we use to calculate the diffracted signal.

3.3. Strain-optic effect in glass substrate

When the grating-shaped acoustic echo is at the glass-Ni interface, part of the acoustic wave is transmitted into the glass substrate, where it continues to propagate away from the interface. The acoustic grating modifies the refractive index in glass due to the strain-optic effect and results in a grating in the optical constants of the glass. Such a quasi-static grating in the glass would give rise to a constant (in time) diffracted signal. Interestingly, the diffraction signal we observe is an oscillating curve (shown by the blue panel of Figs. 4(a) and 4(b)). This can be explained as follows. When the time-delayed probe pulse propagates through the acoustic grating in the glass, light is diffracted in the direction of the detector. The probe pulse continue to propagate and subsequently reflects from the glass-Ni interface. The reflected probe pulse diffracts for the second time from the same acoustic grating in the glass in the same direction. This leads to interference between the electric fields of the diffracted pulses. Whether the interference is constructive or destructive depends on the phase accumulated by the optical pulse before it diffracts a second time. This causes alternate constructive or destructive interference leading to an oscillation of the diffracted signal. Note that as the acoustic velocity in the glass is much smaller than the speed of light in the glass, the acoustic grating can be considered quasi-constant for the probe pulse at a give time delay. Due to multiple round trips of the acoustic wave in Ni, more than one grating-shaped acoustic wave is propagating in the glass substrate after about 100 ps. The probe light can diffract from all these grating-shaped acoustic echoes in the glass. Gradually, the diffraction signal gets weaker due to dispersion and damping of the acoustic wave in the glass.

3.4. Strain-optic effect in Ni

When the grating-shaped acoustic echo arrives at the glass-Ni interface, it also modifies the complex refractive index of Ni near the glass-Ni interface due to the strain-optic effect. This results in a grating in the optical constants. The probe pulse diffracts from this grating, giving rise to a diffracted signal peak each time the grating-shaped acoustic echo arrives at the glass-Ni interface, as shown in the magenta panel of Figs. 4(a) and 4(b). Since this grating is the result of an acoustic wave propagating back and forth inside the Ni layer, the peaks of the diffracted signal are separated by the acoustic round trip time of 45 ps. The transient, periodic (in time) grating at the glass-Ni interface due to strain-optic effect and due to the displacement of the atoms at the glass-Ni interface (shown in the green panel in Figs. 4(a) and 4(b)), always occur simultaneously. However, as the strain-optic coefficient of Ni is small, diffraction due to the strain-optic effect is weak in comparison to the diffraction due to the interface displacement.

3.5. Thermal grating in Ni

The optical pump pulse is absorbed by the Ni layer within the optical penetration depth (13 nm for 400 nm wavelength light), creating a hot electron gas [40]. The hot electron gas cools by heating up the Ni lattice. As Ni has a very high electron-phonon coupling strength, the hot electron gas cools before the energy can diffuse much deeper into the Ni layer [41–45]. As a result, the top layer of Ni heats up with an exponentially decaying temperature gradient in a direction perpendicular to the surface of the Ni layer. Later in time, the heat diffuses even deeper into the metal layer and reaches the buried grating. Due to the difference in diffusion volume above the valleys and the peaks of the buried grating, a spatially periodic temperature pattern is formed, which is also present near the glass-Ni interface. The change in the temperature modifies the complex refractive index of Ni due to the thermo-optic effect and results in a grating in the optical

Optics EXPRESS

constants of Ni. The calculated diffraction signals resulting from this thermal grating are shown in Figs. 4(a) and 4(b) (yellow panels). In both plots, the signal remains zero for approximately 125 ps, and later gradually increases to a quasi-constant value. This is because lattice heat slowly diffuses deeper into the Ni layer, and it takes a finite amount of time before temperature contrast is achieved between areas above the valleys and peaks of the grating. The diffracted signal reaches a constant value when the temperature gradient along the vertical direction vanishes, and a quasi-constant temperature is attained above the valleys and above the peaks of the grating, each at different temperature value. The lateral diffusion of heat does not wash away the thermal grating on the time scale of our experiments (<1 ns) because the thickness of the layer (130 nm) is much smaller than the pitch of the grating (6000 nm). The effects due to lateral lattice heat diffusion are nonetheless taken into account in our numerical model.

3.6. Surface roughness

The most surprising factor that affects the shape and strength of the diffracted signal is the surface roughness of the glass-Ni interface. The random surface roughness of the glass-Ni interface results in the scattering of probe light in all directions. The Si-photodiode placed at the location where we expect the first-order diffracted light from the acoustic gratings, also detects the light scattering in that particular direction. The intensity of the scattered light is constant with respect to time. The random surface scattering needs to be taken into consideration when the intensity of the probe pulse diffracted from the acoustic gratings is comparable to or weaker than the intensity of the randomly scattered light. The intensity of the background scattered light is experimentally measured when the chopper blocks alternating pump pulses and is numerically subtracted from the measured diffracted signal. However, the electric field of the scattered light interferes with the electric field of the diffracted light, and the measured diffracted intensity is the coherent sum of these electric fields. Hence a numerical subtraction of measured signals does not correctly remove the contribution of the scattered light. In our numerical simulations, we add an electric field with a constant amplitude which coherently adds up to the diffracted electric field. In Figs. 4(a) and 4(b) (orange panel) we show the calculated contribution to the diffraction signals for the 2 and 12 nm amplitude buried grating samples, assuming that only the constant electric field we have added is present. The "scattered signals" are constant in time. Although the strength of the constant diffracted field is the same for both samples, their strength with respect to the diffraction signals due to other effects varies. Therefore, in Fig. 4(a), the constant line has a value comparable to that due to other effects and hence has a significant contribution to the total diffracted signal. In Fig. 4(b), we see that the "scattered signal" has a value very close to zero and therefore has an almost negligible contribution to the diffraction signals caused by the other effects. The amplitude of the added electric field is estimated with the help of an analytical scattering model and the details are discussed below.

3.6.1. Surface scattering model: Rayleigh-Rice theory

We use the Rayleigh-Rice scattering theory, to estimate the intensity of the scattered light recorded by the detector [46–49]. The Rayleigh-Rice approach can be used in cases where the Root Mean Square (RMS) roughness of the surface, σ, is much less than the incident optical wavelength λ, that is $\sigma/\lambda<0.01$ [46,49]. To obtain the amount of light scattered towards the detector using Rayleigh-Rice theory, we need to obtain the topography of the surface from which the light scatters. Measuring the roughness profile of the glass-Ni interface directly is not possible with an AFM, hence we measured the roughness profile of the glass substrate and assume that the roughness profile of the glass-Ni interface will follow the glass surface topography. This is a reasonable assumption given that Ni was evaporated at a very slow rate and that Ni atoms have a good affinity for the glass which ensures that the deposited Ni layer will follow the topography of the glass substrate. We measure the topography of the glass substrate for an area of about

Optics EXPRESS

17 μm^2 using an AFM. The measured topography is shown in Fig. 5(a). The RMS roughness of the measured surface was calculated to be 307±5 pm. Using the Rayleigh-Rice scattering theory we can obtain the Angle Resolved Scattering (ARS) by calculating the Power Spectral Density (PSD) function from the measured AFM data. The ARS is defined as the ratio between the power of the scattered light, $P_s(\alpha_s)$, and the power of the incident light, P_i, normalized to a finite solid angle, $\Delta\Omega$ and α_s is the scattering angle with respect to the normal to the scattering surface. Mathematically ARS can be expressed as [46,49,50],

$$ARS(\alpha_s) = \frac{P_s(\alpha_s)}{\Delta\Omega_s P_i}, \tag{1}$$

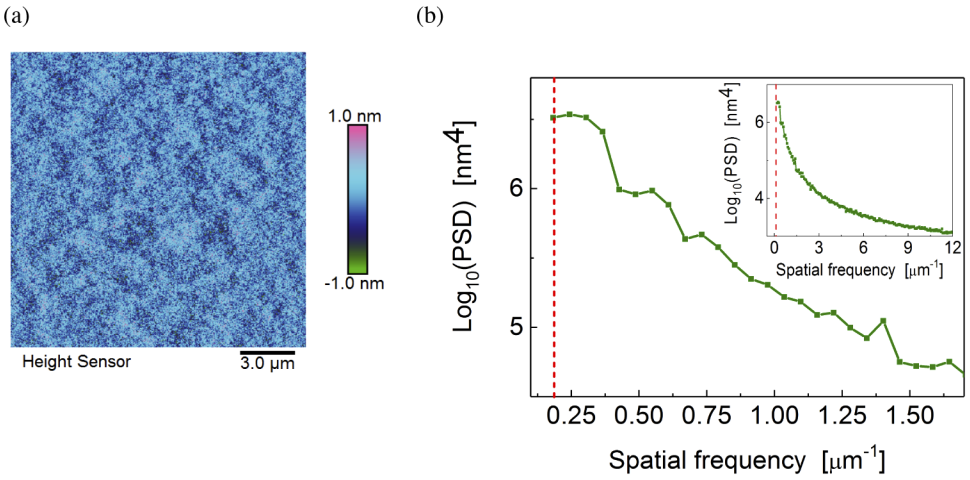

Fig. 5. (a) AFM measurement showing the height profile of the glass surface. (b) PSD vs. spatial frequency calculated from the AFM measurement. The vertical red line marks the spatial frequency of the buried grating

The PSD is a measure of surface roughness which provides information about the different spatial frequency components present in the surface roughness. Mathematically a 2D PSD is the modulus squared of the surface profile's 2D Fourier transform and can be written as,

$$PSD(f_x, f_x) = \lim_{L\to+\infty} \frac{1}{L^2} \left| \int_0^L \int_0^L z(x,y) e^{-2\pi i(f_x x + f_y y)} dxdy \right|^2. \tag{2}$$

Here L is the length of the scanned area, $z(x, y)$ is the surface topography which has a zero mean, and f_x and f_y are the two spatial frequencies components of the surface roughness where x and y are the two in-plane spatial coordinates. In Rayleigh-Rice scattering theory, there is a simple relation between the ARS and the PSD [49,50],

$$ARS(\alpha_s) = Q\frac{16\pi^2}{\lambda^4}\cos(\alpha_i)\cos^2(\alpha_s)PSD(f). \tag{3}$$

Here α_i is the incident angle with respect to the normal to the scattering surface, Q is the polarization-dependent optical reflectance of the scattering surface, and f is the spatial frequency.

In Fig. 5(b) we plot the calculated PSD as a function of the spatial frequency for the surface topography shown in Fig. 5(a). In our experiments, $\alpha_i = 10°$, $\alpha_s = 18°$ and $Q = 0.68$ [40] for $\lambda = 800$ nm. The value for $\Delta\Omega$ is determined by the size of the aperture just in front of the photodiode and it was measured to be approximately 5.5×10^{-6} sr. The detector is placed at an

Optics EXPRESS

angle such that it measures light scattered from a spatial frequency of $0.67\,\mu m^{-1}$, which is the spatial frequency of the buried grating. From Fig. 5(b), the PSD we obtain for the $0.67\,\mu m^{-1}$ spatial frequency is $10^{6.5} = 3.16 \times 10^6$ nm^4. Substituting all these values in Eq. (3), we calculate the ARS to be 6.48×10^{-4}. Using Eq. (1) the light scattering efficiency of rough interface along the direction of the photodetector (P_s/P_i) is calculated to be 3.56×10^{-9}.

Based on the above calculation, we have added a constant electric field along the direction of the first-order diffraction signal in the numerical simulations. The intensity of the scattered light was varied around the expected value of 3.56×10^{-9} times the intensity of the incident probe light. The best match with the measurements was observed when the intensity was 1.56×10^{-9} times the intensity of the incident probe light. The small deviation from the calculated value could be due to errors in the calculation of the PSD. It is known that PSD calculations can have errors due to limitations in accurately measuring large surface areas using an AFM. The finite size of the AFM tip and instrumental artifacts will also add to the error [51]. The phase of the added electric field is adjusted in order to obtain a good fit with the measured data for each sample. We like to point out that, despite having an RMS roughness below 0.5 nm, the contribution of the light scattered from interface roughness cannot be ignored when the diffraction signals are weak. To best of our knowledge, this is the first demonstration of the role of surface roughness in femto/picosecond laser-induced ultrasonics measurements.

3.7. All contributions combined

Although we can numerically calculate the intensity of the diffracted probe pulse for each factor contributing to the diffracted signal, in actual measurements, we can only record the total diffracted intensity. The electric field of the diffracted light in a particular direction is the coherent sum of the diffracted electric fields in that direction. Therefore, the phase differences between all the diffracted electric fields are important. Of the five different effects discussed above, all except the surface roughness are induced by the pump pulse and therefore, will be dependent on the pump-probe delay. These four different effects result in gratings from which the probe pulse diffracts, and the diffracted light can be represented by a single electric field. This electric field can be written as,

$$E_a(r,t) = E_a e^{(\omega t - k\cdot r + \theta_1)}, \tag{4}$$

where E_a, and θ_1 are the pump-probe-delay-dependent amplitude and phase of the electric field, respectively. Note that the time dependence of the envelope of the optical ultra-short pulse is left out from the equation. However, the electric field of the light scattered due to the interface roughness from different samples has a constant amplitude and a constant but random phase. We can consider a rough interface to be the superposition of a large number of sinusoidal phase gratings with different orientations, periods, amplitudes, and phases. Since our detector is placed at a location where we expect the diffracted light from a 6 µm period grating, only roughness gratings with the same spatial frequency scatters light towards the detector. For all samples used in our experiments, we expect the roughness profile at the glass-Ni interface to be similar. Therefore we also expect the amplitude of the scattered electric field to be constant for all samples. However, the phase of the scattered electric field is random and can vary from one sample to another and also from one illumination spot to another on the same sample. Therefore, we can approximate the electric field of the light scattered due to the interface roughness along the direction of the first-order diffracted light as,

$$E_s(r,t) = E_s e^{(\omega t - k\cdot r + \theta_2)}. \tag{5}$$

Here, E_s and θ_2 are the *constant* amplitude and the phase of the electric field, respectively. The measured diffraction signal, which is the total intensity of the light incident on the detector, I, is

Optics EXPRESS

proportional to the square of the total electric field. We can write,

$$I \propto |E_{tot}|^2 \tag{6}$$

where,

$$|E_{tot}|^2 = |E_s + E_a|^2 = |E_s|^2 + |E_a|^2 + 2|E_a||E_s|\cos(\theta_1 - \theta_2). \tag{7}$$

In our measurements, we numerically subtract the probe signal measured by the detector when the chopper blocks the pump pulse, thus removing the terms not induced by the pump pulse. Hence, we observe only terms that contain E_a in Eq. (7). The diffraction signal we plot can thus be expressed as,

$$|E_a|^2 + 2|E_a||E_s|\cos(\theta_1 - \theta_2). \tag{8}$$

Now that we understand the different factors and how they contribute to the diffraction signal, we will explain why the shape of the diffracted signal is different for different samples. As the amplitude of the buried grating increases, the diffraction of the probe light due to pump-induced effects (displacement of the glass-Ni interface, strain-optic effect in Ni, thermo-optic effect in Ni and strain-optic effect in glass) gets stronger. However, the scattering of light due to the interface roughness is independent of the buried grating amplitude. In the cases of samples with 6 and 12 nm amplitude buried gratings, the diffraction from the gratings induced by the pump pulse (acoustic gratings and thermal grating) is strong (see Fig. 4(b)). As a result, $|E_a|$ is much larger than $|E_s|$ in the relation shown in Eq. (8). Therefore, in these measurements, the intensity of the light diffracted due to the gratings induced by the pump pulse, i.e., $|E_a|^2$, dominates the measured total signal. In the measured diffraction signal for 6 and 12 nm buried grating samples, the peak in diffraction signal at 46±1 ps is mostly due to the displacement of the interface. The oscillation that follows until about 200 ps is mainly due to the combined effect of the strain-optic effect and the displacement of the interface. After 200 ps, the strain-optic effect in the glass and the thermo-optic effect dominates. The slow, gradual increase in the offset of the diffracted signal is explained by the formation of the thermal grating due to the thermo-optic effect.

For the samples with 0.5, and 2 nm amplitude buried gratings, $|E_a|$ is comparable to $|E_s|$ because the intensity of probe light diffracted from the gratings induced by the pump pulse is comparable to the intensity of the scattered probe light (see Fig. 4(a)). Hence, we observe the term $|E_a|^2 + 2|E_a||E_s|\cos(\theta_1 - \theta_2)$ from the relation shown in Eq. (8). As the grating-shaped acoustic wave propagates through the glass, the time-dependent phase of the diffracted light periodically changes between 0 and π. As a result, the value of $\cos(\theta_1 - \theta_2)$ oscillates periodically above and below zero and can result in a value of $|E_a|^2 + 2|E_a||E_s|\cos(\theta_1 - \theta_2) < 0$. This causes the "negative" diffraction signal observed in the measurements of 2 nm, and 0.5 nm amplitude buried gratings. For these measurements, the role of pump-induced effects (displacement, strain-optic effects, and thermo-optic effect) is similar to that of 12 and 6 nm buried grating samples. The only difference is the *relatively* low contribution of pump-induced effects compared to light scattered from the interface roughness, which makes the measured diffraction signal become negative. As a result, the overall shape of the diffracted signal looks different.

The diffraction efficiency as a function of grating amplitude is expected to be quadratic if the surface roughness does not play any role, or if the acoustic wavelength is larger than the buried grating amplitude. For small-amplitude buried gratings, a deviation from quadratic behavior is expected because in this case the diffracted optical field is weak and interferes with scattered light. Due to the random nature of the phase of the scattered light, the strength of the total diffracted signal will be random. When the buried grating amplitude is larger than the length of the acoustic wave, the first diffraction peak will be caused only by that part of the acoustic wave that reflects off the peaks of the buried grating and arrives at the surface first. For increasing buried grating amplitudes, the diffraction signal due to this first acoustic echo will not increase. When the grating amplitude is between these scenarios, we expect to see a quadratic dependence.

Optics EXPRESS

4. Conclusion

We have shown that it is possible to detect gratings with peak-to-valley amplitudes as small as 0.5 nm, underneath a 130 nm thick Ni layer, using laser-induced ultrasound. The diffraction of the probe pulse is due to displacement of the interface, the strain-optic effect, and thermo-optic effect. Our model accurately predicts the shape of the time-dependent diffracted signal, and we explain how the shape of the measured signal is affected by the different physical effects. The light scattered from the interface due to small roughness (<307 pm RMS) plays a very important role in understanding the measurements as the scattered optical electric field adds coherently to the optical fields diffracted by the acoustic waves. Scattered light should be taken into account when the strength of the diffracted probe light is comparable to that of the scattered light.

Funding

Advanced Research Center for Nanolithography; Vrije Universiteit Amsterdam; Universiteit van Amsterdam; Nederlandse Organisatie voor Wetenschappelijk Onderzoek.

Disclosures

The authors declare no conflicts of interest.

References

1. C. Thomsen, H. T. Grahn, H. J. Maris, and J. Tauc, "Surface generation and detection of phonons by picosecond light pulses," Phys. Rev. B **34**(6), 4129–4138 (1986).
2. O. Matsuda, M. C. Larciprete, R. L. Voti, and O. B. Wright, "Fundamentals of picosecond laser ultrasonics," Ultrasonics **56**, 3–20 (2015).
3. P. Ruello and V. E. Gusev, "Physical mechanisms of coherent acoustic phonons generation by ultrafast laser action," Ultrasonics **56**, 21–35 (2015).
4. T. F. Crimmins, A. A. Maznev, and K. A. Nelson, "Transient grating measurements of picosecond acoustic pulses in metal films," Appl. Phys. Lett. **74**(9), 1344–1346 (1999).
5. A. Devos, "Colored ultrafast acoustics: From fundamentals to applications," Ultrasonics **56**, 90–97 (2015).
6. O. B. Wright and K. Kawashima, "Coherent phonon detection from ultrafast surface vibrations," Phys. Rev. Lett. **69**(11), 1668–1671 (1992).
7. M. Kouyaté, T. Pezeril, V. Gusev, and O. Matsuda, "Theory for optical detection of picosecond shear acoustic gratings," J. Opt. Soc. Am. B **33**(12), 2634–2648 (2016).
8. R. M. Slayton and K. A. Nelson, "Picosecond acoustic transmission measurements. i. transient grating generation and detection of acoustic responses in thin metal films," J. Chem. Phys. **120**(8), 3908–3918 (2004).
9. T. Saito, O. Matsuda, and O. B. Wright, "Picosecond acoustic phonon pulse generation in nickel and chromium," Phys. Rev. B **67**(20), 205421 (2003).
10. O. B. Wright and V. E. Gusev, "Acoustic generation in crystalline silicon with femtosecond optical pulses," Appl. Phys. Lett. **66**(10), 1190–1192 (1995).
11. T. Saito, O. Matsuda, M. Tomoda, and O. B. Wright, "Imaging gigahertz surface acoustic waves through the photoelastic effect," J. Opt. Soc. Am. B **27**(12), 2632–2638 (2010).
12. R. M. Slayton, K. A. Nelson, and A. A. Maznev, "Transient grating measurements of film thickness in multilayer metal films," J. Appl. Phys. **90**(9), 4392–4402 (2001).
13. M. Lejman, V. Shalagatskyi, O. Kovalenko, T. Pezeril, V. V. Temnov, and P. Ruello, "Ultrafast optical detection of coherent acoustic phonons emission driven by superdiffusive hot electrons," J. Opt. Soc. Am. B **31**(2), 282 (2014).
14. K. E. O'Hara, X. Hu, and D. G. Cahill, "Characterization of nanostructured metal films by picosecond acoustics and interferometry," J. Appl. Phys. **90**(9), 4852–4858 (2001).
15. D. Yarotski, E. Fu, L. Yan, Q. Jia, Y. Wang, A. J. Taylor, and B. P. Uberuaga, "Characterization of irradiation damage distribution near tio2/srtio3 interfaces using coherent acoustic phonon interferometry," Appl. Phys. Lett. **100**(25), 251603 (2012).
16. A. Steigerwald, Y. Xu, J. Qi, J. Gregory, X. Liu, J. K. Furdyna, K. Varga, A. B. Hmelo, G. Lupke, L. C. Feldman, and N. Tolk, "Semiconductor point defect concentration profiles measured using coherent acoustic phonon waves," Appl. Phys. Lett. **94**(11), 111910 (2009).
17. T. Dehoux, K. Ishikawa, P. H. Otsuka, M. Tomoda, O. Matsuda, M. Fujiwara, S. Takeuchi, I. A. Veres, V. E. Gusev, and O. B. Wright, "Optical tracking of picosecond coherent phonon pulse focusing inside a sub-micron object," Light: Sci. Appl. **5**(5), e16082 (2016).
18. K. A. Nelson, R. J. D. Miller, D. R. Lutz, and M. D. Fayer, "Optical generation of tunable ultrasonic waves," J. Appl. Phys. **53**(2), 1144–1149 (1982).

Optics EXPRESS

19. T. Pezeril, P. Ruello, S. Gougeon, N. Chigarev, D. Mounier, J.-M. Breteau, P. Picart, and V. Gusev, "Generation and detection of plane coherent shear picosecond acoustic pulses by lasers: Experiment and theory," Phys. Rev. B **75**(17), 174307 (2007).
20. P. Babilotte, P. Ruello, D. Mounier, T. Pezeril, G. Vaudel, M. Edely, J.-M. Breteau, V. Gusev, and K. Blary, "Femtosecond laser generation and detection of high-frequency acoustic phonons in gaas semiconductors," Phys. Rev. B **81**(24), 245207 (2010).
21. O. B. Wright, "Ultrafast nonequilibrium stress generation in gold and silver," Phys. Rev. B **49**(14), 9985–9988 (1994).
22. B. Bonello, B. Perrin, E. Romatet, and J. Jeannet, "Application of the picosecond ultrasonic technique to the study of elastic and time-resolved thermal properties of materials," Ultrasonics **35**(3), 223–231 (1997).
23. F. Pérez-Cota, R. J. Smith, E. Moradi, L. Marques, K. F. Webb, and M. Clark, "High resolution 3D imaging of living cells with sub-optical wavelength phonons," Sci. Rep. **6**, 1–11 (2016).
24. J. A. Guggenheim, J. Li, T. J. Allen, R. J. Colchester, S. Noimark, O. Ogunlade, I. P. Parkin, I. Papakonstantinou, A. E. Desjardins, E. Z. Zhang, and P. C. Beard, "Ultrasensitive plano-concave optical microresonators for ultrasound sensing," Nat. Photonics **11**(11), 714–719 (2017).
25. J. A. Guggenheim, T. J. Allen, A. Plumb, E. Z. Zhang, M. Rodriguez-Justo, S. Punwani, and P. C. Beard, "Photoacoustic imaging of human lymph nodes with endogenous lipid and hemoglobin contrast," J. Biomed. Opt. **20**(05), 1–3 (2015).
26. J. Brunker and P. Beard, "Velocity measurements in whole blood using acoustic resolution photoacoustic doppler," Biomed. Opt. Express **7**(7), 2789–2806 (2016).
27. A. P. Jathoul, J. Laufer, O. Ogunlade, B. Treeby, B. Cox, E. Zhang, P. Johnson, A. R. Pizzey, B. Philip, T. Marafioti, M. F. Lythgoe, R. B. Pedley, M. A. Pule, and P. Beard, "Deep in vivo photoacoustic imaging of mammalian tissues using a tyrosinase-based genetic reporter," Nat. Photonics **9**(4), 239–246 (2015).
28. G. Leahu, E. Petronijevic, A. Belardini, M. Centini, R. Li Voti, T. Hakkarainen, E. Koivusalo, M. Guina, and C. Sibilia, "Photo-acoustic spectroscopy revealing resonant absorption of self-assembled gaas-based nanowires," Sci. Rep. **7**(1), 2833 (2017).
29. E. Petronijevic, G. Leahu, V. Mussi, C. Sibilia, and F. A. Bovino, "Photoacoustic technique for the characterization of plasmonic properties of 2d periodic arrays of gold nanoholes," AIP Adv. **7**(2), 025210 (2017).
30. T. Pozar, J. Lalos, A. Babnik, R. Petkovsek, M. Bethune-Waddell, K. J. Chau, G. V. B. Lukasievicz, and N. G. C. Astrath, "Isolated detection of elastic waves driven by the momentum of light," Nat. Commun. **9**(1), 3340 (2018).
31. P. Burgholzer, M. Thor, J. Gruber, and G. Mayr, "Three-dimensional thermographic imaging using a virtual wave concept," J. Appl. Phys. **121**(10), 105102 (2017).
32. T. W. Murray, M. Haltmeier, T. Berer, E. Leiss-Holzinger, and P. Burgholzer, "Super-resolution photoacoustic microscopy using blind structured illumination," Optica **4**(1), 17–22 (2017).
33. A. J. den Boef, "Optical wafer metrology sensors for process-robust CD and overlay control in semiconductor device manufacturing," Surf. Topogr.: Metrol. Prop. **4**, 023001 (2016).
34. J.-M. Han, "Architecture and method for nand flash memory," (2008). US Patent 7,372,715.
35. D. Resnati, A. Goda, G. Nicosia, C. Miccoli, A. S. Spinelli, and C. M. Compagnoni, "Temperature effects in nand flash memories: A comparison between 2-d and 3-d arrays," IEEE Electron Device Lett. **38**(4), 461–464 (2017).
36. H. Kim, S.-J. Ahn, Y. G. Shin, K. Lee, and E. Jung, *Evolution of NAND flash memory: From 2D to 3D as a storage market leader* (IEEE, 2017), pp. 1–4.
37. J. Alsmeier, "Ultrahigh density vertical nand memory device," (2012). US Patent 8,198,672.
38. S. Edward, H. Zhang, I. Setija, V. Verrina, A. Antoncecchi, S. Witte, and P. Planken, "Detection of Hidden Gratings through Multilayer Nanostructures Using Light and Sound," Phys. Rev. Appl. **14**(1), 014015 (2020).
39. H. Zhang, A. Antoncecchi, S. Edward, I. Setija, P. Planken, and S. Witte, "Unraveling phononic, optoacoustic, and mechanical properties of metals with light-driven hypersound," Phys. Rev. Appl. **13**(1), 014010 (2020).
40. P. B. Johnson and R. W. Christy, "Optical constants of transition metals: Ti, V, Cr, Mn, Fe, Co, Ni, and Pd," Phys. Rev. B **9**(12), 5056–5070 (1974).
41. J. Hohlfeld, S.-S. Wellershoff, J. Güdde, U. Conrad, V. Jähnke, and E. Matthias, "Electron and lattice dynamics following optical excitation of metals," Chem. Phys. **251**(1-3), 237–258 (2000).
42. J. Güdde, J. Hohlfeld, J. Müller, and E. Matthias, "Damage threshold dependence on electron–phonon coupling in Au and Ni films," Appl. Surf. Sci. **127-129**, 40–45 (1998).
43. M. Bonn, D. N. Denzler, S. Funk, M. Wolf, S.-S. Wellershoff, and J. Hohlfeld, "Ultrafast electron dynamics at metal surfaces: Competition between electron-phonon coupling and hot-electron transport," Phys. Rev. B **61**(2), 1101–1105 (2000).
44. S.-S. Wellershoff, J. Güdde, J. Hohlfeld, J. Muller, and E. Matthias, "Role of electron-phonon coupling in femtosecond laser damage of metals," Proc. SPIE **3343**, 378–387 (1998).
45. E. Beaurepaire, J.-C. Merle, A. Daunois, and J.-Y. Bigot, "Ultrafast spin dynamics in ferromagnetic nickel," Phys. Rev. Lett. **76**(22), 4250–4253 (1996).
46. J. C. Stover, *Vector scattering theory* (SPIE Press, 1995).
47. J. M. Elson and J. M. Bennett, "Vector scattering theory," Opt. Eng. **18**(2), 116–124 (1979).
48. S. O. Rice, "Reflection of electromagnetic waves from slightly rough surfaces," Comm. Pure Appl. Math. **4**(2-3), 351–378 (1951).
49. S. Schröder, A. Duparré, L. Coriand, A. Tünnermann, D. H. Penalver, and J. E. Harvey, "Modeling of light scattering in different regimes of surface roughness," Opt. Express **19**(10), 9820–9835 (2011).

Optics EXPRESS

50. T. V. Vorburger, E. Marx, and T. R. Lettieri, "Regimes of surface roughness measurable with light scattering," Appl. Opt. **32**(19), 3401–3408 (1993).
51. T. D. B. Jacobs, T. Junge, and L. Pastewka, "Quantitative characterization of surface topography using spectral analysis," Surf. Topogr.: Metrol. Prop. **5**, 013001 (2017).